In situ electrochemical synchrotron radiation for Li-ion batteries

Tibebu Alemu[a] and Fu-Ming Wang[b,a]*

[a]Graduate Institute of Applied Science and Technology, National Taiwan University of Science and Technology, Taipei, Taiwan, and [b]Sustainable Energy Center, Graduate Institute of Applied Science and Technology, National Taiwan University of Science and Technology, Taipei, Taiwan. *Correspondence e-mail: mccabe@mail.ntust.edu.tw

Observing the electronic structure, compositional change and morphological evolution of the surface and interface of a battery during operation provides essential information for developing new electrode materials for Li-ion batteries (LIBs); this is because such observations demonstrate the fundamental reactions occurring inside the electrode materials. Moreover, obtaining detailed data on chemical phase changes and distributions by analyzing an operating LIB is the most effective method for exploring the intercalation/de-intercalation process, kinetics and the relationship between phase change or phase distribution and battery performance, as well as for further optimizing the material synthesis routes for advanced battery materials. However, most conventional in situ electrochemical techniques (other than by using synchrotron radiation) cannot clearly or precisely demonstrate structural change, electron valence change and chemical mapping information. In situ electrochemical-synchrotron radiation techniques such as X-ray absorption spectroscopy, X-ray diffraction spectroscopy and transmission X-ray microscopy can deliver accurate information regarding LIBs. This paper reviews studies regarding various applications of in situ electrochemical-synchrotron radiation such as crystallographic transformation, oxidation-state changes, characterization of the solid electrolyte interphase and Li-dendrite growth mechanism during the intercalation/de-intercalation process. The paper also presents the findings of previous review articles and the future direction of these methods.

1. Introduction to in situ synchrotron techniques

The construction of third-generation synchrotrons with high brilliance and low emittance at the end of the 1990s facilitated the development of new in situ techniques (Bleith et al., 2015). In situ synchrotron radiation techniques can be performed during operations and provide real-time system application through synchrotron X-ray sources. Synchrotron radiation is also applicable for studying real-time structural changes occurring on the surface or bulk of materials in Li-ion batteries (LIBs) undergoing intercalation/de-intercalation. An extensive study on the electron-valance change of transition-metal (TM) cathode materials was conducted to elucidate the mechanisms of the reactions occurring during cycling (Wang, Wu et al., 2013). Among numerous synchrotron techniques, X-ray absorption spectroscopy (XAS), X-ray diffraction spectroscopy (XRD) and transmission X-ray microscopy (TXM) are the core synchrotron techniques for in situ operations. Since the emerging of in situ XAS (Nakai et al., 1999), there have been several scientific advances recorded (Domantovskii et al., 2006). XAS measures the energy dependence of the X-ray absorption coefficient at and above the absorption edge. Based on the purpose of the investiga-

Figure labels: Mylar Sheet, Gasket, Bolt Holes, Anode, Cathode, X-ray Window, Separator, Bolt Holes, Al Blocks
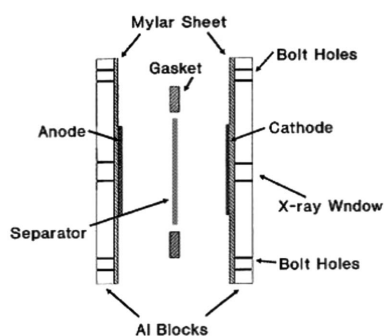
tion, one can use either hard XAS to examine the oxidation state, site symmetries, coordination number, covalent bond length and local structure of TM ions (Ates *et al.*, 2014; Kim *et al.*, 2005), or soft XAS to investigate the electronic configuration of low-atomic-weight ions in electrode materials (Wang *et al.*, 2007). As reported in previous review papers, *in situ* XRD studies have revealed highly valuable information regarding numerous ordered atomic structures in a variety of common materials (Morcrette *et al.*, 2002). Consequently, XRD testing provides information on structural change such as average grain size, crystallinity, strain and crystal defects (Choi *et al.*, 2012). Additionally, TXM is the synchrotron-based full-field imaging method that acquires a complete image on a direct imaging base with the highest resolution and is the best suited for morphological studies on dynamic events and microtomography (Kaulich *et al.*, 2009). It can also perform two-dimensional imaging on several materials such as fuel cells and battery electrodes and has received increasing interest for applications in different fields of study (Li *et al.*, 2016; Singh *et al.*, 2012; Wang, Chen-Wiegart *et al.*, 2013).

This paper reviews the progression of *in situ* electrochemical-synchrotron methods in the field of most promising energy storage devices, especially LIBs (Bashash *et al.*, 2011; He *et al.*, 2012; Kojima *et al.*, 2009). LIBs are typically manufactured to provide improved high-power density using high-energy active materials. To realise the wide use of LIBs, further improvement in energy density, power capability, calendar-life performance, safety and reduction in costs are necessary. *In situ* synchrotron characterization techniques were actively developed worldwide to address these challenges. Combining all the aforementioned *in situ* synchrotron techniques can simplify the complexity of LIBs by improving the understanding of intercalation/de-intercalation reaction mechanisms and battery degradation processes that engenders capacity loss and battery failure. The advantage of understanding such mechanisms and processes is that it facilitates investigation of the chemical properties, structural elucidation and phase transformations, thus rendering the study of LIBs highly valuable (Nelson *et al.*, 2013). Therefore, the present review paper discusses the fundamental principles and applications of XAS, including X-ray absorption fine structure (XAFS) and extended X-ray absorption fine structure (EXAFS), as well as XRD and TXM. These powerful techniques are selectively revised in this paper as a result of their ability to examine the electronic structure, oxidation-state changes, configuration changes and image probing during the charging and discharging of LIBs on the electrode surface and interface. The relevant literature is also highlighted.

2. X-ray absorption spectroscopy

2.1. *In situ* synchrotron XANES experiments

X-ray methods involve numerous techniques and applications based on the scattering, emission and absorption properties of the X-ray radiation. The detailed theory and working principles of XAS were described by Giorgetti *et al.* (1999)

and Ye *et al.* (2016). An X-ray absorption spectrum can be divided into two regions, X-ray absorption near-edge structure (XANES) and extended X-ray absorption fine-structure (EXAFS), which originate from different physical-chemical mechanisms (Wang *et al.*, 2014a). The XANES is the part of the X-ray absorption spectrum that is in the immediate surroundings of the absorption edge, approximately ±50 eV from the edge. XANES is highly sensitive to chemical bonding, exhibiting an average oxidation state (Schnohr & Ridgway, 2015; Westre *et al.*, 1997), local coordination environment and electronic structure (Choi *et al.*, 2002), but it is not usually analyzed quantitatively. Absorption measurements for LIB materials are usually conducted at the *K*-edge, the absorption of 1*s* core states. Measurements at the *K*-edge are most suitable for elements of low atomic number and for first-row TMs in order to track the oxidation change. Pre-edge structures (De Groot *et al.*, 2009) are generally observed in the rising area of the *K*-edge spectra of first-row TMs from 1*s*–3*d* electronic transitions. Multiple analyses have been conducted on the 1*s*–3*d* component of the Fe *K*-edge (Westre *et al.*, 1997) and several other metals (Giuli *et al.*, 2005). *In situ* XAS experiments were carried out in the transmission mode using methods described by Giorgetti *et al.* (1999) and its spectroelectrochemical cell design is shown in Fig. 1. Discs were punched from the anodes and cathodes of the disassembled cells. The cathode active material was $Li_{1.023}Ni_{0.872}Co_{0.151}O_{2.05}$. The anode formulation was 75% carbon (Osaka Gas MCMB-6-2800), 16.5% graphite flake (Timcal SFG-6) and 8.5% PVDF (Kureha #c). The active material was removed from one side of the current collector prior to assembly in the cell. The overall cell pack consisted of the anode, cathode, a fresh Celgard separator and electrolyte (1 *M* $LiPF_6$ in a 1:1 EC:DMC solvent). The cell was housed between two machined blocks of aluminium. The aluminium blocks were machined to provide X-ray windows and holes for bolts. The windows were sheets of 250 μm Mylar. A rubber gasket was used to form a hermetic seal. Provisions were made for current collection by using thin strips of copper and aluminium. XAS scans covering both the Co and Ni *K*-edges while charging the
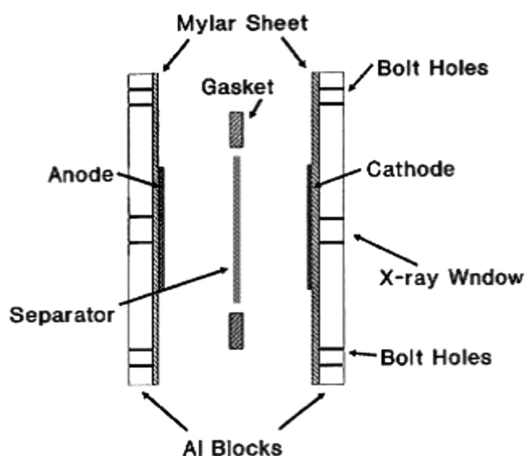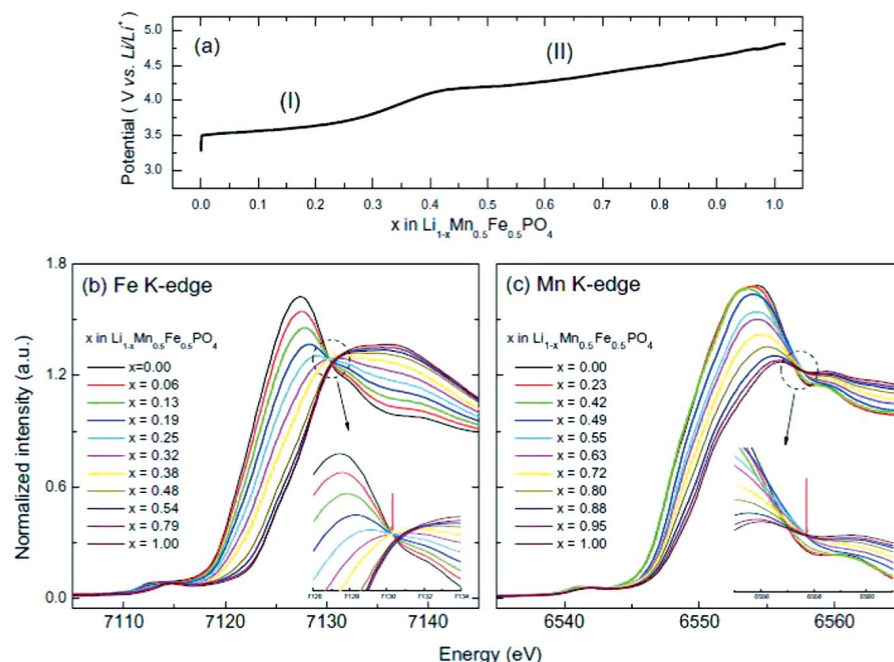

Figure 1
The spectroelectrochemical cell. Reprinted from Balasubramanian *et al.* (2001), with permission from Elsevier.

cell at the C/2 rate were stated in the paper (Balasubramanian *et al.*, 2001).

The following examples realise the precision of the XANES experiments in reaction mechanism description during charging of LIBs. The first one is the electronic structure and the local environment of charge compensation mechanisms on a $Li_{1-x}Co_{1/3}Ni_{1/3}Mn_{1/3}O_2$ electrode system mentioned by Yoon *et al.* (2005) and reviewed by McBreen (2009). Accordingly, the Mn XANES spectrum was reported to be similar to that of $Li_{1.2}Cr_{0.4}Mn_{0.4}O_2$ and $LiNi_{0.5}Mn_{0.5}O_2$ electrode materials, signifying that the oxidation state was maintained as Mn^{4+} throughout charging. However, the Ni K-edge XANES spectra shifted to higher energies during charging and therefore the charge compensation at the metal site during Li de-intercalation was achieved mainly through the oxidation of Ni^{2+}/Ni^{4+} ions. However, Co K-edge spectra were more complicated and were not interpreted in the paper. An O K-edge XANES spectrum was also provided by Yoon *et al.* (2005). Similarly, a phase transition behavior study explored the electrochemical Li extraction of carbon-coated $Li_{1-x}Mn_{0.5}Fe_{0.5}PO_4$ (Nam, Yoon *et al.*, 2009). In the first charge profile of C-$Li_{1-x}Mn_{0.5}Fe_{0.5}PO_4$ based on *in situ* XAS experiments, two voltage plateaus were observed at approximately 3.6 and 4.2 V, marked as (I) and (II) in the charge profile, respectively (Fig. 2*a*). The *in situ* Fe and Mn K-edge spectra are shown in Figs. 2(*b*) and 2(*c*), respectively. The spectra clearly illustrated that the Fe K-edge shifted toward higher energy during the first plateau, and the Mn K-edge displayed in the second plateau, indicating that the voltage plateaus at approximately 3.6 and 4.2 V mainly originated from the redox reactions of Fe^{2+}/Fe^{3+} and Mn^{2+}/Mn^{3+}, respectively. This result agrees well with previous studies (Li *et al.*, 2002; Yamada *et al.*, 2001). However, two notable findings were revealed in the *in situ* XANES results. First, two single isosbestic points [represented by red arrows in the insets of Figs. 2(*b*) and 2(*c*)] appeared in some Fe and Mn K-edge XANES spectra. These points indicate that spectra with composition ranges of $0.00 \leq x \leq 0.38$ observed for the Fe K-edge and $0.49 \leq x \leq 1.00$ for the Mn K-edge have isosbestic points at approximately 7130 and 6558 eV, respectively. C-$Li_{1-x}Mn_{0.5}Fe_{0.5}PO_4$ has a single isosbestic point. In these individual composition changes, the species involved in the chemical reaction (recognized by oxidation change) is independently Fe and Mn and not the intermixing of them. Nonetheless, the second narrow composition range ($0.4 \leq x \leq 0.5$) confirms that the Fe^{2+}/Fe^{3+} and Mn^{2+}/Mn^{3+} redox reactions occurred simultaneously. Therefore, the absence of an isosbestic point in the XANES spectra indicates the presence of more reacting species during

Figure 2
(*a*) First-charge curves of C-$Li_{1-x}Mn_{0.5}Fe_{0.5}PO_4$ at a C/20 rate and corresponding *in situ* (*b*) Fe and (*c*) Mn K-edge XANES spectra. Reprinted from Nam, Yoon *et al.* (2009), with permission from Elsevier.

the reaction (Wang *et al.*, 2004). For example, $LiFe_{1/4}Mn_{1/4}Co_{1/4}Ni_{1/4}PO_4$/C is cathode material similar to C-$Li_{1-x}Mn_{0.5}Fe_{0.5}PO_4$ except for the presence of Co and Ni metal compositions. Fig. 3 shows the first charge profiles of $LiFe_{1/4}Mn_{1/4}Co_{1/4}Ni_{1/4}PO_4$/C up to ~5.0 V at a C/7 rate (Nam, Wang *et al.*, 2009). Three voltage plateaus at around 3.6, 4.2 and 4.7 V (marked as I, II and III) can be clearly seen in Fig. 3. The nominal capacity of the first charge is 180 mAh g^{-1}. The normalized *in situ* XANES spectra for Fe, Mn, Co and Ni K-edges are plotted in Fig. 4.

The capacity change between the consecutive scans is ~5 mAh g^{-1}. The main edge shift to higher energy in its K-edge XANES spectra indicates the increase in the average oxidation state of this element. Figs. 4(*a*)–4(*c*) evidently show the edge shifts in the Fe, Mn and Co K-edge regions toward
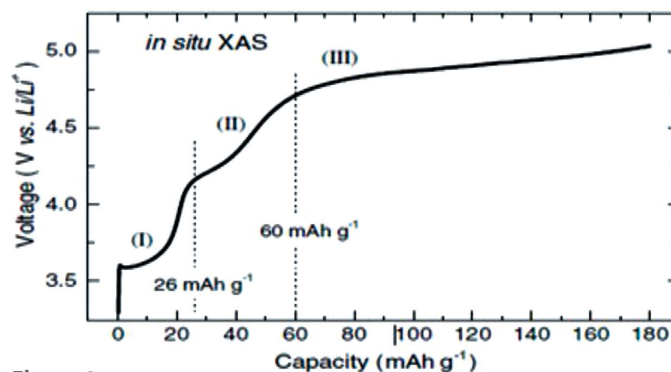
Figure 3
First charge curves of the $LiFe_{1/4}Mn_{1/4}Co_{1/4}Ni_{1/4}PO_4$/C cathode at a C/7 rate during *in situ* XAS. Reprinted from Nam, Yoon *et al.* (2009), with permission from Elsevier.
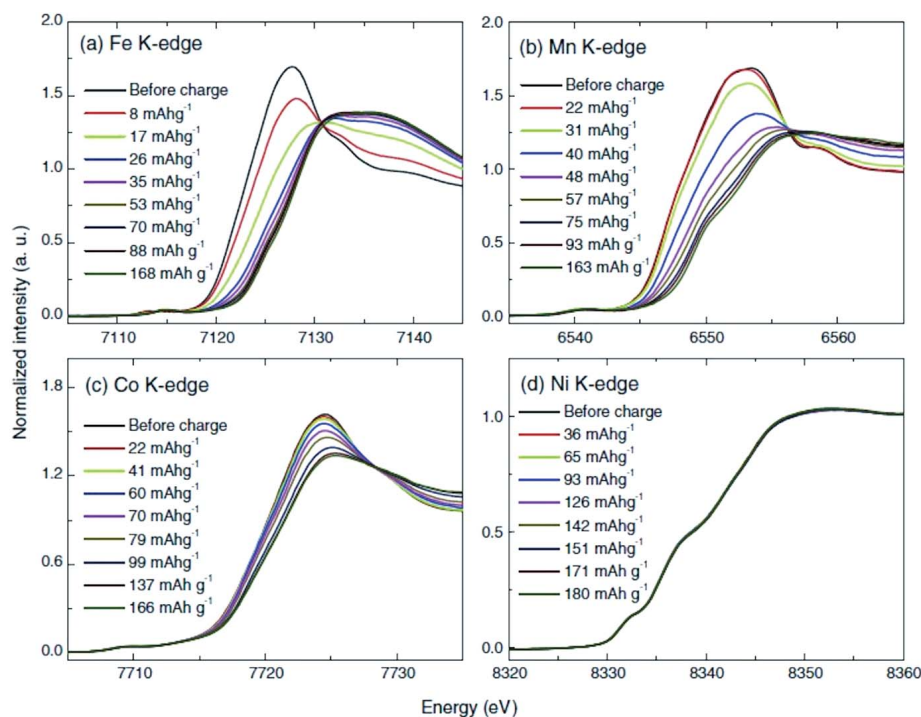
Figure 4
Normalized *in situ* Fe, Mn, Co and Ni K-edge XANES spectra of LiFe$_{1/4}$Mn$_{1/4}$Co$_{1/4}$Ni$_{1/4}$PO$_4$/C during the first charge. Reprinted from Nam, Yoon *et al.* (2009), with permission from Elsevier.

demonstrate that oxidation occurred in successive two-phase transitions between 3 and 4.5 V (Chen *et al.*, 2007, 2009). *In operando* XANES characterization for V$_2$O$_5$/graphene (V$_2$O$_5$-G) was performed to describe the oxidation state of vanadium. On the insertion of the Li$^+$ ions into V$_2$O$_5$-G, the K-edge of the vanadium continuously shifted towards lower binding energies. This shift indicates a decrease in the average valence state of vanadium, which corresponds to an increase in the number of inserted Li$^+$ ions in each V$_2$O$_5$. At the fully discharged state, an emerging shoulder was found, which is consistent with the reduction of V^{+4} to V^{+3} (Mansour *et al.*, 2003). The XANES K-edge and pre-edge shift as a function of Li composition in V$_2$O$_5$-G were also shown by Liu, Liu *et al.* (2014). Obviously, both the K-edge and pre-edge energy shifts varied linearly with the valence of the vanadium atom. Importantly, the energy shifts during the charging process also showed a linear change, which confirms the electronic reversibility of the hybrid (Raccichini *et al.*, 2015).

higher energy positions, indicating the increase of oxidation states of the Fe, Mn and Co ions at different charge states. In the first plateau (I) region at ∼3.6 V (capacity from 0 to ∼26 mAh g^{-1}), most of the Fe K-edge shift occurs, and then the Mn K-edge shifts take over in the second plateau (II) region at ∼4.2 V (from ∼22 to ∼50 mAh g^{-1}). In the early parts of the third plateau (III) region at ∼4.7 V (capacity from ∼55 to ∼100 mAh g^{-1}), the Co K-edge starts to shift. Therefore, three voltage plateaus at around 3.6, 4.2 and 4.7 V during the first charge are mainly correlated with the redox reactions of Fe^{2+}/Fe^{3+}, Mn^{2+}/Mn^{3+} and Co^{2+}/Co^{3+}, sequentially. Therefore, the Fe K-edge, Mn K-edge and Co K-edge have a single isosbestic point at approximately 7130, 6558 and 7728 eV, respectively. The same absorption phenomena as shown by Nam, Yoon *et al.* (2009) have been observed in the absence of Co and Ni K-edge.

On the other hand, there were no changes of the Ni K-edge region as observed in Fig. 4(*d*). This shows that the apparent voltage plateau at around 4.9 V in Fig. 3 does not originate from the Ni^{2+}/Ni^{3+} redox reaction, but very likely from the electrolyte decomposition at high voltages. As illustrated, electrolytes with an electrochemical stability above 5 V are optimal for studying the Ni^{2+}/Ni^{3+} reaction mechanism. Recently, the functioning of Li$_3$V$_2$(PO$_4$)$_3$ (LVP) (Kim *et al.*, 2016) and other vanadium-containing cathodes in LIBs at the atomic level has been investigated (Wang, Liu *et al.*, 2012; Wang *et al.*, 2014b; Du *et al.*, 2012). When LVP was cycled from 3 to 4.5 V, three distinct plateaus were observed at approximately 3.6, 3.7 and 4.1 V *versus* Li/Li$^+$, which was attributed to the oxidation of V^{3+}/V$^{3.25+}$, V$^{3.25+}$/V$^{3.5+}$ and V$^{3.5+}$/V^{4+}, respectively (Kim *et al.*, 2016). The three well defined plateaus

In situ Fe K-edge XAS spectra were collected and the charge–discharge cycling was performed to ensure complete conversion and re-conversion reactions in the FeO$_{0.7}$F$_{1.3}$/C electrode (Sina *et al.*, 2013) as well. The XANES spectra clearly indicate the rigid edge shift toward lower energy in a continuous manner which corresponds to a continuous voltage decrease from 3.5 to 2.1 V, revealing the oxidation state change from Fe$^{2.7+}$/Fe^{2+} through lithium insertion into the rutile FeO$_{0.7}$F$_{1.3}$ phase in LIBs. For the voltage plateau at ∼2.0 V, the spectra do not show rigid edge shifting but profile distorting centered on an isosbestic point located at ∼7121 eV. The spectra change in the opposite manner to the spectral changes, confirming the reversible reconversion reactions between Fe and the lithiated iron oxyfluoride phase. However, it should be noted that the isosbestic point in this region is slightly shifted to higher energy compared with that during discharge. This confirms that different reaction pathways exist during the reconversion process even though the exact composition of the lithiated phase in this region is unknown. The entire edge continuously shifted back to higher energies, indicating the continuous increase of the average Fe oxidation state *via* lithium extraction from the lithiated phase during reconversion reaction over ∼3.1 V (Sina *et al.*, 2013). In the above descriptions, the synchrotron-based *in situ* XANES technique is attempted to study oxidation state changes of TMs in various cathode materials of LIBs. Clear edge-shifts in the Fe, Mn and Co K-edge XANES for cathode materials were recorded. Consequently, there are three voltage plateaus observed during the first charge which mainly correlate to an

average oxidation change of Fe^{2+}/Fe^{3+}, Mn^{2+}/Mn^{3+} and Co^{2+}/Co^{3+}, sequentially for those cathode materials containing Fe, Mn and Co metal compositions, respectively. In general, on the insertion of the Li^+ ions, the spectral edge of the metal may shift towards lower binding energies corresponding to the decrease in the average valence state and *vice versa*.

2.2. Solid electrolyte interphase characterization through XANES

A passive surface layer is known to almost fully cover both the anode and cathode in LIBs and is thus generally called the solid electrolyte interphase (SEI). Peled (1979) introduced the application of this layer to alkali and alkaline earth metals in organic electrolytes. SEI formation has been observed in various electrode materials (Araki & Sato, 2003; Kong *et al.*, 2001; Möller *et al.*, 2003). The SEI layer is a key factor in the electrochemical performance and calendar life of LIBs because it prevents the electrode surface from further reacting with the electrolyte components (Arora *et al.*, 1998). Additionally, a Li^+-conducting and electronically insulating SEI layer (Peled *et al.*, 2011) prevents continual electrolyte reduction and Li consumption during cycling (Schranzhofer *et al.*, 2006; Yamada *et al.*, 2009). However, the formation of a non-uniform SEI layer can cause non-uniform Li deposition and the formation of Li dendrites (Crowther & West, 2008), which can engender battery internal short and failure (Aurbach *et al.*, 2000). *In situ* electrochemical synchrotron radiation is crucial for understanding the SEI formation reaction mechanisms in LIBs because the actual SEI formation occurs during the first cycle (Gauthier *et al.*, 2015). Experimentally, the SEI has been premeditated using a variety of *in situ* methods (Lipson *et al.*, 2011; McArthur *et al.*, 2012), and other studies have also been conducted to probe its composition and morphology (Blyth *et al.*, 2000; Andersson & Edström, 2001). These studies have revealed that SEI formation on the anode surface is more pronounced than that on the cathode, and its composition depends on the choice of electrolyte and electrode materials. Certain additives have been reported to improve the interface between the electrode and electrolyte, thus improving battery performance. For example, a Li–oxysulfite film (Li_2SO_3 and $ROSO_2Li$) was formed by the reductive decomposition of an ethylenesulfite (ES) additive on graphite in a $LiPF_6$/propylene carbonate (PC) and ES electrolyte (Ota *et al.*, 2003). These films contribute to the SEI layer, which can

transport Li^+ but prevents electron transfer. An S K-edge XANES process was conducted on the local structure of an S atom in a film formed on a graphite anode and $LiCoO_2$ cathode in an ES-additive electrolyte. Fig. 5 depicts the S K-edge XANES spectra of some S reagents and the SEI layer formed on the graphite anode and the $LiCoO_2$ cathode in a 1 M $LiPF_6$/PC + ES 5% electrolyte. Accordingly, the SEI layer formed on the graphite anode contained four peaks (2471.9, 2473.3, 2477.6 and 2480.4 eV). Strong peaks were observed at 2477.6 and 2480.4 eV, which were attributed to Li_2SO_3 and $ROSO_2Li$, respectively, because they correspond to the Na_2SO_3 and n-$C_7H_{15}OSO_2Na$ spectra, respectively. The sulfate in Li_2SO_4 and that in Na_2SO_4 were observed at 2482.3 eV. The S K-edge XANES spectra changed minimally due to the difference in counter cations such as Li and Na. The S K-edge XANES spectrum of ES exhibited two peaks, at 2476.3 and 2478.1 eV. In addition, the S K-edge XANES spectrum of Na_2S displayed four peaks (2471.2, 2478.4, 2480.2 and 2482.0 eV), whereas that of S produced only one peak (2472.1 eV). The S K-edge XANES spectrum of di-n-propyl-disulfide (R–S–S–R) presented two peaks (2471.9 and 2473.4 eV) while diphenyldisulfide (Ph–S–S–Ph) displayed two peaks (2472.2 and 2473.9 eV), and dimethylsulfide (C–S–C) showed one peak (2473.9 eV). Finally, the diphenylsulfide
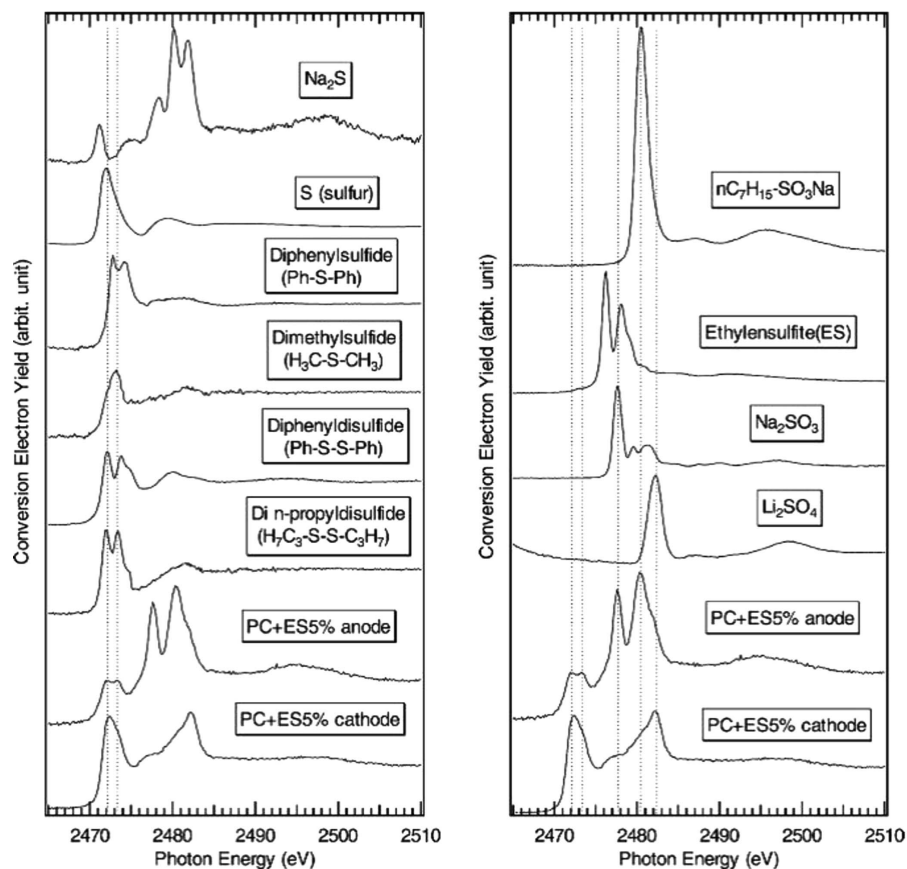

Figure 5
S K-edge XANES spectra of standard S reagents and SEI layers on the graphite anode and the $LiCoO_2$ cathode in 1 M $LiPF_6$/PC + ES 5% electrolyte. Reprinted from Ota *et al.* (2003), with permission from Elsevier.

(Ph–S–Ph) spectrum showed two peaks, at 2472.8 and 2474.2 eV.

Synchrotron-based hard X-ray diffraction and spectroscopy (>5 keV) have already become extremely valuable in modern material research and are routinely used to characterize energy materials. However, soft X-ray spectroscopy (SXS), an established powerful tool for fundamental physics and chemistry research, has not been fully utilized in material science. This is mainly due to the strict vacuum requirement and shallow probing depth (ranges from angstroms to hundreds of nanometers) of many soft X-ray (<3 keV) characterization tools which has hindered its application on practical systems under *in situ/operando* conditions. SXS techniques can provide information on both the occupied and unoccupied electronic states. They are inherently sensitive to the element, orbital and different atomic sites in the material of low-atomic-weight ions (De Groot & Kotani, 2008; Wang *et al.*, 2007). Balasubramanian *et al.* (2002) reported the *in situ* soft XAS measurements for the Ni $L_{3,2}$-edges, Co $L_{3,2}$-edges, O K-edges and F K-edge in the energy range 500–950 eV. The soft X-ray absorption measurements were performed at beamline U7A of the National Synchrotron Light Source (NSLS) at Brookhaven National Laboratory (BNL) (Fischer & DeKoven, 1996). The estimated incident X-ray resolution was $\sim$0.15 eV at the O K-edge and $\sim$0.45 eV at the Ni $L_{3,2}$-edges. Fig. 6 shows a total-electron-yield XAS spectrum for an as-received $LiNi_{0.85}Co_{0.15}O_2$ powder sample over the energy range 525–950 eV. The edge-steps which arise from the Co and Ni $L_{3,2}$-edges and O K-edge are marked in Fig. 6(*a*). The two additional sharp features observed at $\sim$574 and 583 eV above the O K-edge correspond to the absorption features from Cr (Cr underlies the gold coating of the beamline X-ray optics). Fig. 6(*b*) shows a similar spectrum for the as-prepared fresh electrode except for the addition of the F K-edge at 685 eV due to the presence of the PVDF binder.

Fig. 7(*a*) shows a spectrum for a sample taken from a cell cycled at 60% state of charge (SOC) with a 9% ΔSOC swing, for two weeks at 70°C. It was observed that there are major changes at the O and F K-edges for the cycled electrodes. Also, the signals at the Co and Ni L-edges are greatly attenuated. The spectra for all cycled electrodes were similar, except in the degree to which the Co and Ni L-edge step-jumps were attenuated. This appeared to be a random process that bore no relationship to cycling conditions. Fig. 7(*b*) shows a spectrum for LiF which is
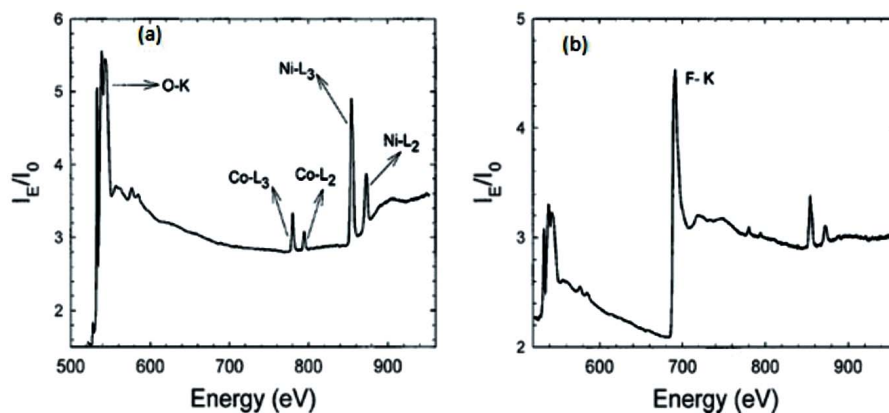

Figure 6
Total-electron-yield XAS spectrum for (*a*) $LiNi_{0.85}Co_{0.15}O_2$ and (*b*) as-prepared fresh $LiNi_{0.85}Co_{0.15}O_2$ electrode. Reprinted with permission from Balasubramanian *et al.* (2002). Copyright 2002, The Electrochemical Society.

similar to the F K-edge spectrum for the cycled electrode. Balasubramanian *et al.* (2002) recognized that the most likely source of LiF comes from the decomposition of $LiPF_6$,

$$LiPF_6 \longrightarrow PF_5 + LiF. \tag{1}$$
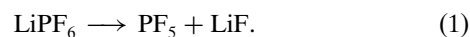
A similar reaction mechanism was described by Sloop *et al.* (2001) at 85°C and they noted that the role of the electrodes in this reaction is unknown. The precipitated LiF is the most likely major contributor to the insulating layer found on cycled electrodes. The precipitation of LiF could affect ionic motion by pore plugging, or could contribute to resistive electrical paths to parts of the cathode structure. LiF is also known to form at the anode surface; however, it is most likely entrained in an organic gel of polymeric electrolyte decomposition products and does not form a dense coating that significantly increases electrode impedance. At the cathode, organic decomposition products are unstable, particularly on charged cathodes. This permits the formation of a dense LiF film coating (Balasubramanian *et al.*, 2002). Therefore, based on the purpose of the investigation, we can use either hard XAS to examine the oxidation state of TM for high-atomic-

Figure 7
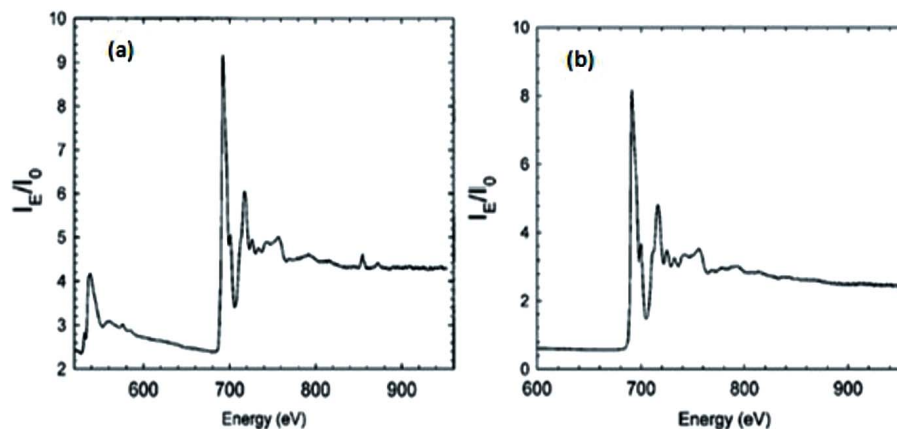Total-electron-yield XAS spectrum for (*a*) $LiNi_{0.85}Co_{0.15}O_2$ electrode cycled at 60% SOC, 9% ΔSOC for two weeks at 70°C, (*b*) LiF. Reprinted with permission from Balasubramanian *et al.* (2002). Copyright 2002, The Electrochemical Society.

weight ions (Nam, Wang *et al.*, 2009) or soft XAS to investigate the electronic configuration of low-atomic-weight ions in electrode materials (Wang *et al.*, 2007; Balasubramanian *et al.*, 2002). The above experiments signify that *in situ* hard/soft XAS is a valuable surface/interface chemistry characterization tool in the study of SEI formation on the cathode/anode materials.

2.3. *In situ* synchrotron EXAFS experiments

The EXAFS is also part of an X-ray spectrum and provides quantitative structural information (Rehr & Albers, 2000); it does not require long-range order and is applicable to a wide range of ordered and disordered materials (Zabinsky *et al.*, 1995). The energy of the emitted electron, the incoming photon energy and the binding energy of the electron are correlated with definite mathematical formula described by Willmott *et al.* (2013). The self-interference of the photoelectron wave oscillates between constructive and destructive interference at the absorbing atom. This modulates the total absorption after the edge. The oscillation exhibits a frequency in space, which corresponds to a certain interatomic distance between a defined set of atoms in real space. The measured absorption is the atomic absorption modulated by the changes induced by the local structure and can be described by equations given by Koningsberger *et al.* (2000). An EXAFS study was conducted to elucidate the mechanism of the reaction of Li with CoO regarding the local geometric and electronic structures (Choi *et al.*, 2002). Li_yCoO_2, in which y is the Li content, was used to investigate the Co K-edge EXAFS properties during the first cycle, in addition to the use of Co K-edge XAS, Co $L_{2,3}$-edge and oxygen K-edge XAS for electronic structure analysis. Figs. 8(*a*) and 8(*b*) show k^3-weighted $\chi(k)$ spectra and their Fourier transforms (FTs) for the Li_yCoO_2 system, respectively. The principal peaks of the FTs between 1.0 and 6.0 Å in Fig. 8(*b*) provide vital structural information because the FT peaks are closely associated with the site symmetry surrounding the central Co atom. The authors described that for pristine CoO the FT peak at approximately 1.7 Å corresponded to six coordinated O atoms, the nearest neighbors of the Co atom, whereas the peak at approximately 2.6 Å was assigned to the contribution of 12 coordinated Co atoms in the next edge-shared octahedral site (Laruelle *et al.*, 2001). The results reveal that the main contribution to the FT magnitude of approximately 3.9 Å was from the double-scattering path of Co → O → Co in the corner-shared octahedral. The FT magnitudes at approximately 4.8 and 5.6 Å were attributed to the single-scattering path of Co → Co and the focused double scattering of Co → Co → Co in the edge-shared octahedral layer, respectively (Galoisy *et al.*, 2001). As illustrated in Fig. 8(*b*), the electrochemical insertion of Li⁺ up to 0.78 mol reduced the magnitude of the FT peaks of pure CoO without affecting the overall spectral shape. Generally, local structural parameters such as particle size and coordination number are linearly dependent on the FT peak intensity in the EXAFS. The FT peak intensities at 3.9, 4.8 and 5.6 Å decreased dramatically when

0.78 mol of Li⁺ was inserted into CoO. However, the FT peak intensities at 3.9, 4.8 and 5.6 Å decreased with those of the CoO, and their spectral features remained as previously described, indicating that the high-temperature cubic phase was maintained despite the insertion of Li⁺. Therefore, the insertion of Li⁺ reduces the size of particles containing CoO.

As presented in Fig. 8(*b*), for insertions of Li⁺ equal to or above 1.32 mol, the major change in the FT was the evolution
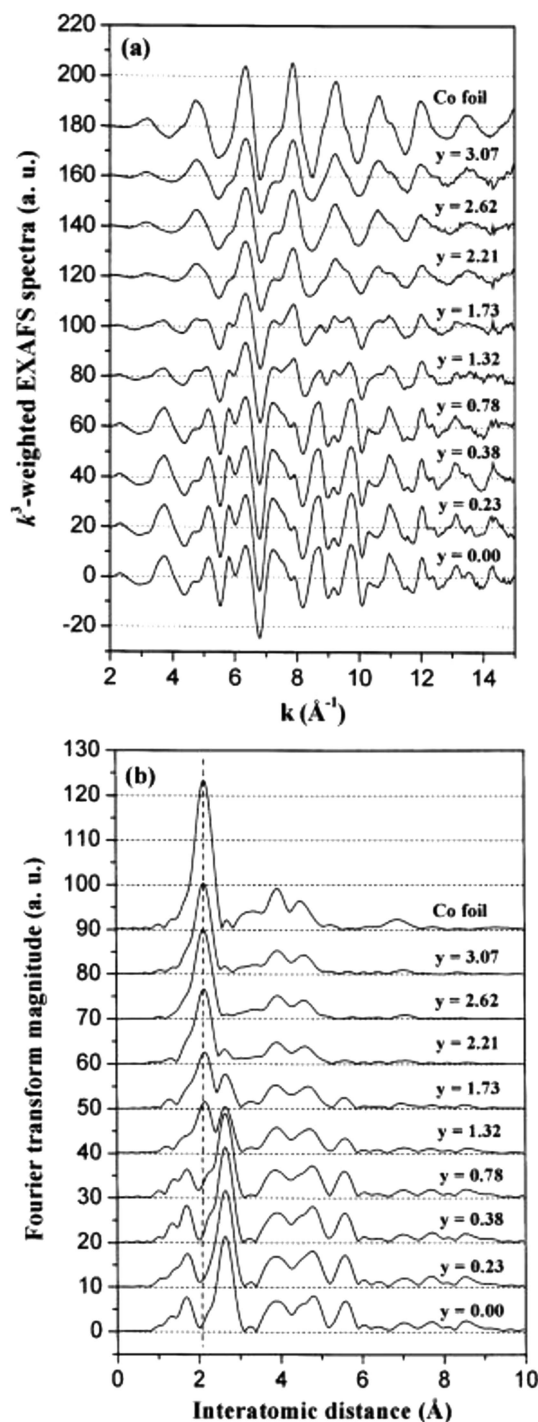
Figure 8
(*a*) Co K-edge $k^3\chi(k)$ spectra and (*b*) their FTs for the electrochemically Li-ion-inserted Li_yCoO_2 system. Reprinted with permission from Choi *et al.* (2002). Copyright (2002) American Chemical Society.

of a new peak at approximately 2.1 Å. This new peak is characteristic of the reduced Co^0 phase and corresponds to six coordinated Co atoms, the ne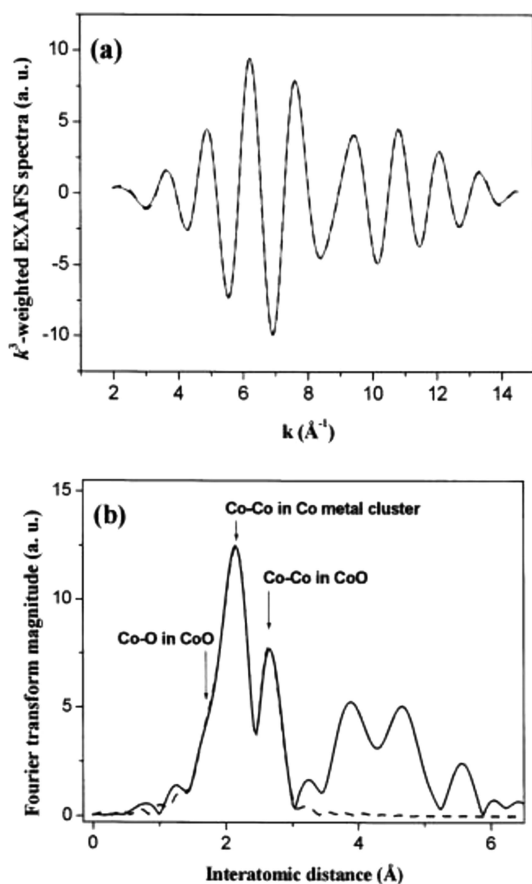arest neighbors of the Co atom (Laruelle *et al.*, 2001). The emergence of this peak was therefore engendered by the gradual formation of metallic Co^0 in the Li_yCoO_2 system. For the Li^+ insertions equal to or above 2.62 mol (Fig. 8*b*), the FT peak corresponding to the edge-shared $Co \rightarrow Co$ single scattering in CoO at approximately 2.5 Å almost disappeared. Further insertion of Li^+ up to 3.07 mol did not affect the local structure of the Co^0 phase; thus, the formation of the Co^0 phase terminated when the Li content was approximately 2.62 mol. Their results are consistent with the following reaction defining the electrochemical reaction (Tarascon, 2010),

$$2Li^+ + CoO + 2e^- \longrightarrow Li_2O + Co. \qquad (2)$$
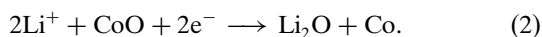
Quantitative information on the cobalt site in the lithiated CoO was obtained by simulating experimental EXAFS spectra by using the *FEFF* code in the single-scattering region. Figs. 9(*a*) and 9(*b*) show the experimental Fourier-filtered $k^3\chi(k)$ spectra and FTs (solid line) and the best-fit $k^3\chi(k)$ spectra and FTs (dotted line) for $Li_{1.73}CoO_2$, respectively. The effects of the Li atom on the EXAFS signal were not considered in the theoretical scattering calculations because the backscattering amplitude of the photoelectron of the Li atom was extremely weak. The coordination numbers of the CoO and Co phases in $Li_{1.73}CoO_2$ were approximately half (Co–O in CoO), a third (Co–Co in CoO) and a half (Co–Co in Co foil) of the total values. Because the surface-to-volume ratio and the number of distorted sites on the surface increased as particle size decreased, the number of neighboring atoms corresponding to each bonding pair decreased linearly. These results indicate that the two phases were distributed independently with a smaller particle size than that of the bulk CoO and Co foil (Choi *et al.*, 2002).

3. X-ray diffraction phenomena

In situ XRD studies can be carried out in the transmission mode as indicated by *in situ* synchrotron XRD in combination with XAS for studying the chemical and structural behavior of $Li_{1.023}Ni_{0.872}Co_{0.151}O_{2.05}$ and its spectroelectrochemical cell (shown in Fig. 1). In order to collect data in transmission mode, the beam has to pass through the $Li_{1.023}Ni_{0.872}Co_{0.151}O_{2.05}$ and Cu foil current collector. Co, Ni and Cu are adjacent first-row transition metals with their respective *K* absorption edges. To minimize absorption, the X-rays should have an energy either below the Co *K*-edge or above the Cu *K*-edge. This particular experiment uses a beam energy of 17.688 keV (0.700 Å), which is above the *K*-edge, and increases the spatial resolution of the detector (Balasubramanian *et al.*, 2001). Despite its high applicability to LIB, *in situ* XRD was conducted in transmission mode for as-synthesized oxides to investigate the local structure and composition of $Li_{1.2}Ni_{0.2}Mn_{0.6}O_2$. Most of the diffraction peaks in the XRD patterns could be indexed according to the α-NaFeO$_2$ ($R\bar{3}m$) structure, with the lattice constants a = 0.2854 nm and c = 1.4225 nm in the hexagonal representation. In addition to the reflections of the $R\bar{3}m$ structure, a set of small relatively broad peaks were visible in the 2θ range 20°–25°. These peaks are characteristic of cation ordering in TM layers, as occurs between the Li and Mn ions in Li_2MnO_3, where a hexagonal (flower-like) arrangement of Li-ions in the TM planes reduces the symmetry of the system to a monoclinic ($C2/m$) system (Bréger *et al.*, 2005). Therefore, the extra peaks in this 2θ range can be indexed to the (020), (110) and (11$\bar{1}$) lattice planes with monoclinic ($C2/m$) symmetry, as in the Li_2MnO_3 unit cell. Fig. 10(*a*) shows the first charge profiles of $LiFe_{1/4}Mn_{1/4}Co_{1/4}Ni_{1/4}PO_4$/C up to ~5.0 V at a C/7 rate during XRD measurements for the same cathode material as used by Nam, Wang *et al.* (2009). Three voltage plateaus at around 3.6, 4.2 and 4.7 V (marked as I, II and III) can be clearly seen which agree well with Wang *et al.* (2008). The *in situ* XRD patterns are plotted in Fig. 10(*b*) covering 2θ angles with three Bragg peaks (200), (311) and (212) (*Pnma* space group). The numbers marked beside the patterns correspond to the scan numbers on the first charge curve in Fig. 10(*a*). The structure marked as phase 1 is for $LiFe_{1/4}Mn_{1/4}Co_{1/4}Ni_{1/4}PO_4$/C before charge showing the same olivine structure as uncharged $LiFePO_4$; however, upon charging, the structural changes of $LiFe_{1/4}Mn_{1/4}Co_{1/4}Ni_{1/4}PO_4$/

Figure 9
(*a*) Experimental Fourier-filtered $k^3\chi(k)$ spectra and FTs (solid line) and (*b*) best-fitted $k^3\chi(k)$ spectra and FTs (dashed line) for $Li_{1.73}CoO_2$, respectively. Reprinted with permission from Choi *et al.* (2002). Copyright (2002) American Chemical Society.
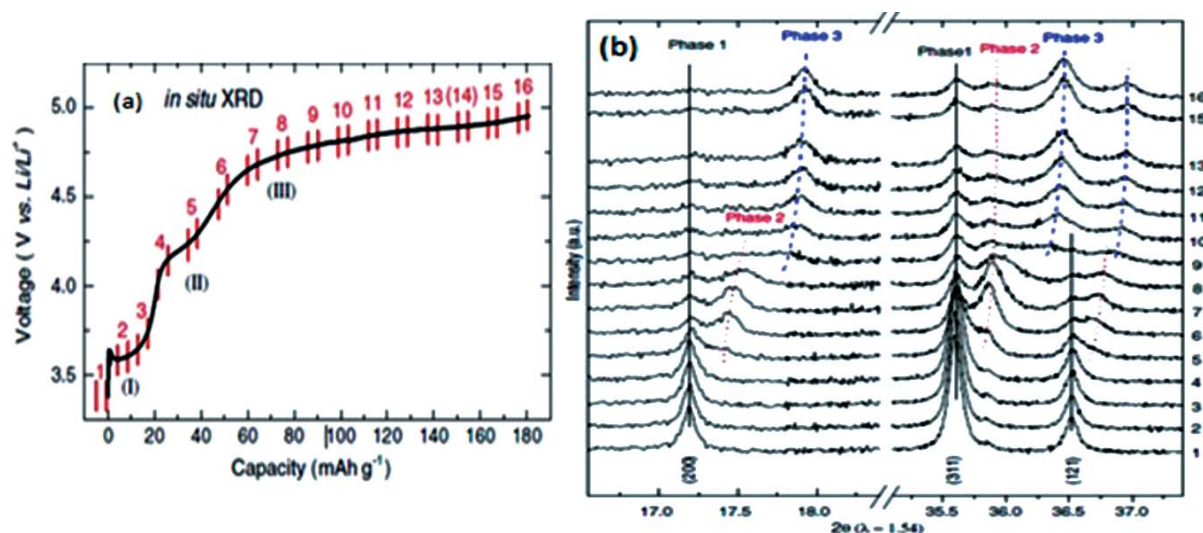
Figure 10
(*a*) First charge curves at a C/7 rate. (*b*) *In situ* XRD patterns for the LiFe$_{1/4}$Mn$_{1/4}$Co$_{1/4}$Ni$_{1/4}$PO$_4$/C cathode. Reprinted from Wang *et al.* (2008), with permission from Elsevier.

C are quite different (Shin *et al.*, 2008; Andersson *et al.*, 2000). At about scan 5, Bragg peaks of a new intermediate phase 2 appeared at slightly higher 2θ values with growing intensities up to scan 9. After that, the formation of the final structure of phase 3 starts and continues to grow through the end of charge. The phases 2 and 3 also have the same olivine structure as phase 1 but different lattice parameters. Similar to LiFePO$_4$, the positions of peaks representing phase 1 do not change noticeably during charge. In contrast, the positions of peaks representing phases 2 and 3 shift toward higher angles during charge, indicating the existence of solid solution regions of these two phases, which is quite different from the case of the FePO$_4$ end phase. Small residues of phases 1 and 2 can be observed in the (200) and (311) reflections at the end of the charge.

These residues show that the phase transitions were not fully completed at the end of charge. It is also interesting to point out, from scans 2 to 4, that no significant changes in the XRD patterns were observed. Scans 2 to 4 were collected during the first plateau at 3.6 V with a capacity of $\sim$20 mAh g^{-1}. At the same time, the Fe K-edge XANES spectra in Fig. 4(*a*) show that most of the Fe^{2+} ions were oxidized to Fe^{3+} in this first plateau region. These results indicate that the electronic structural changes follow the lithium extraction quite well to balance the electrical neutrality. On the other hand, the bulk crystal structural changes, which depend on the Li-ion diffusion and the re-adjustment of the metal phosphate skeleton structure, could lag behind the electrochemical process. Although this type of delayed phase transformation in LiFePO$_4$ during the initial charge has been reported by Chang *et al.* (2008), no information about the oxidation state change of Fe was given. The improvements from the emerging new *in situ* synchrotron radiation techniques, by combining XRD and XAS results for instance (Figs. 4 and 10), have been demonstrated for the LiFe$_{1/4}$Mn$_{1/4}$Co$_{1/4}$Ni$_{1/4}$PO$_4$/C cathode for example, where both

electronic and crystal structure changes have been shown to agree satisfactorily with each other.

The same is true for the C-Li$_{1-x}$Mn$_{0.5}$Fe$_{0.5}$PO$_4$ study combining *in situ* XRD and XAS techniques (Nam, Yoon *et al.*, 2009). To study the Li extraction mechanism more thoroughly, the structural changes of C-Li$_{1-x}$Mn$_{0.5}$Fe$_{0.5}$PO$_4$ were monitored using *in situ* XRD (electronic structural change was mentioned in Fig. 2). Selected *in situ* XRD patterns collected at a C/20 rate during the first charge are presented in Fig. 11. The figure indicates that these patterns contain two 2θ-angle ranges with three Bragg peaks: (200), (020) and (301); moreover, corresponding Li composition x in C-Li$_{1-x}$Mn$_{0.5}$Fe$_{0.5}$PO$_4$ is marked beside each pattern. The structure marked phase 1 corresponds to C-Li$_{1-x}$Mn$_{0.5}$Fe$_{0.5}$PO$_4$ before charge and displays the same olivine-structured phase as uncharged LiFePO$_4$. However, upon charging, the structural changes of
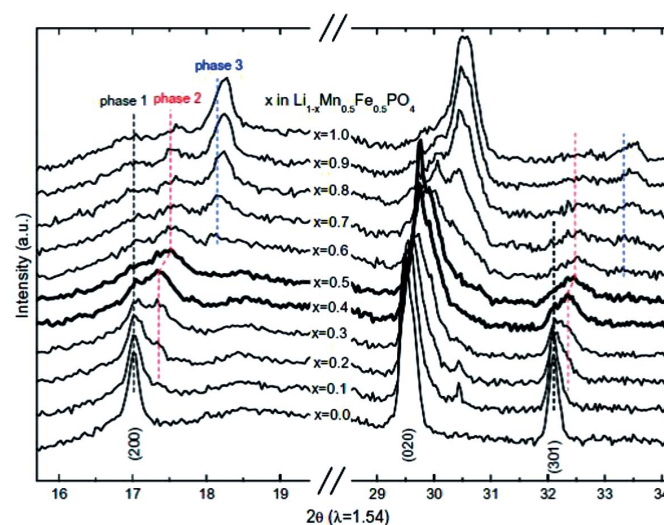

Figure 11
In situ XRD patterns of C-Li$_{1-x}$Mn$_{0.5}$Fe$_{0.5}$PO$_4$ during the first charge. Reprinted from Nam, Yoon *et al.* (2009), with permission from Elsevier.

C-Li$_{1-x}$Mn$_{0.5}$Fe$_{0.5}$PO$_4$ were found to be considerably different from those inherent in the well established two-phase Li extraction process of LiFePO$_4$ (Shin *et al.*, 2008; Andersson *et al.*, 2000). Two new olivine-like phases (phases 2 and 3) were observed during Li extraction, revealing two two-phase reaction mechanisms in certain Li composition ranges. Fig. 2(*a*) depicts C-Li$_{1-x}$Mn$_{0.5}$Fe$_{0.5}$PO$_4$ in the composition range $0.0 \leq x \leq 0.4$ during the early stage of charging. Bragg peaks associated with a new intermediate phase (phase 2) appeared at slightly higher 2θ values with growing intensities that coexisted with the pristine phase (phase 1). The phase 1 and phase 2 Bragg peaks were extremely close to each other, indicating highly similar lattice parameters. In the latter region ($0.5 \leq x \leq 1.0$ in C-Li$_{1-x}$Mn$_{0.5}$Fe$_{0.5}$PO$_4$), phases 2 and 3 coexisted and counteracted. This result is consistent with with the *in situ* XANES results illustrated in Fig. 2 (Nam, Yoon *et al.*, 2009). Similar to LiFePO$_4$, the positions of phase 1 pristine peaks exhibited no noticeable changes, whereas the positions of phase 2 and phase 3 peaks displayed slight shifts toward higher angles. Notably, in the narrow 0.4–0.5 composition range of C-Li$_{1-x}$Mn$_{0.5}$Fe$_{0.5}$PO$_4$, the phase 2 Bragg peaks demonstrated a more significant shift to higher 2θ values compared with those in other composition ranges (Fig. 11), revealing that the single-phase reaction mechanism was dominant in this region. In this narrow composition range ($0.40 \leq x \leq 0.50$ in C-Li$_{1-x}$Mn$_{0.5}$Fe$_{0.5}$PO$_4$) simultaneous redox reactions of Fe^{2+}/Fe^{3+} and Mn^{2+}/Mn^{3+} occurred during Li extraction (Nam, Yoon *et al.*, 2009). The results are in accordance with the reported phase transition behavior of Li$_{1-x}$Fe$_{0.4}$Mn$_{0.6}$PO$_4$ that was observed using synchrotron *in situ* XRD (Bramnik *et al.*, 2005), but they contradict the results of *ex situ* XRD conducted on Li$_{1-x}$Mn$_y$Fe$_{1-y}$PO$_4$ (Molenda *et al.*, 2006, 2007).

A combination of *in situ* synchrotron XRD measurements and local TEM–EELS analysis of individual particles is also applicable. Such techniques can be demonstrated by providing a step-by-step account of the phase evolution and morphological changes occurring in Si nanoparticles with lithiation. The XRD patterns, derived after background subtraction and intensity renormalization, exhibited two major diffraction peaks, namely Si (220) and Si (311), at approximately 9.47° and 11.10°, respectively. Overall, the two diffraction peaks became weaker and wider with lithiation, but were invariant during charging; these results reveal the electrochemical amorphization of the crystalline Si matrix (Wang, Wu *et al.*, 2013). A recent study involving simultaneous *in situ* XAS and XRD on Fe$_{0.5}$TiOPO$_4$ also provided experimental evidence for these techniques. The results were obtained using a newly developed *in situ* cell, which enabled executing nearly simultaneous rapidly alternating *in situ* XRD and XAS measurements. According to the results, reaction with the first Li$^+$ ion per formula unit reduced Ti^{4+}/Ti^{3+}. Concurrently, the formation of a new phase in a two-phase process was detected by *in situ* XRD. Therefore, Bleith *et al.* (2015) conclude that a possible LiFe$_{0.5}$TiOPO$_4$ phase is formed through an insertion reaction. Additionally, a novel investigation on the structural changes occurring on commercially available A123 18650

LiFePO$_4$ during the charge/discharge process have employed *operando* synchrotron high-energy XRD (Liu, He *et al.*, 2014). From the above examples, we can recognize that the experimental results from coupling both methods (*in situ* electrochemical synchrotron XAS and XRD) yield highly precise and correlated data as realised in phase transition phenomena shown by the formation of intermediate phases through the oxidation change of Fe^{2+}/Fe^{3+}, Mn^{2+}/Mn^{3+} and Co^{2+}/Co^{3+} in the case of LiFe$_{1/4}$Mn$_{1/4}$Co$_{1/4}$Ni$_{1/4}$PO$_4$/C.

4. Transmission X-ray microscopy

Synchrotron X-ray imaging techniques are of increasing interest for application in the energy field (Tatsuma *et al.*, 1999) for the reason that synchrotron X-ray imaging is non-destructive, element-sensitive, environmentally friendly and highly penetrating. *In situ* TXM has a high X-ray penetration, and therefore can provide high-quality images with high resolution. A vital and unique capability of *in situ* TXM techniques is that they can provide the oxidation state, electronic and local environment with sub-30 nm spatial resolution rather than only averaged information from conventional spectroscopy (Wang, Karen Chen *et al.*, 2012). By collecting morphological information during cycling, and tuning the X-ray energy at one cycling state across an absorption edge of an element of interest that generates a series of X-ray absorption spectra, TXM enables study of the correlation between the morphology evolution and the chemical phase change under *in situ* conditions.

TXM analysis has utilized the beamline 01B1 facility of the National Synchrotron Radiation Research Center (NSRRC) in Taiwan, and results from a detailed study of the SnO electrode analyzed during the first two lithiation–delithiation cycles have been published (Chao, Yen *et al.*, 2011). Within the past few years, the importance of high-resolution *in situ* X-ray microscopy for studying high-capacity secondary batteries has become apparent (Nelson *et al.*, 2013; Chao, Song *et al.*, 2011; Chao *et al.*, 2010; Wang, Chen-Wiegart *et al.*, 2013). *In situ* TXM research in combination with XANES on battery materials was carried out to achieve the necessary characterization of the phase and chemical states as well as the morphology evolution at nanometer resolution (Wang, Chen-Wiegart *et al.*, 2013). For example, the dynamics of lithiated–delithiated CuO volume expansion are illustrated in Fig. 12. During the first lithiation, CuO particles continuously develop into a core-shell structure with a gray shell, a dark core and an interface phase [Figs. 12*a*–12(*d*)]. As lithiation increases, the shell propagates inwards and the core shrinks further. This core–shell structure is a typical characteristic of the electrochemical interfacial conversion reaction within LIBs. In contrast to these CuO particles, small CuO particles undergo a faster volume change, demonstrating the classic core–shell kinetic theory on the time required for a system to be lithiated. During this time interval (rest period), the morphology of lithiated CuO continues to undergo change (Fig. 12*e*), and the shell thickens. This phenomenon may be attributed to Li$^+$ diffusion and equilibrium within active material particles
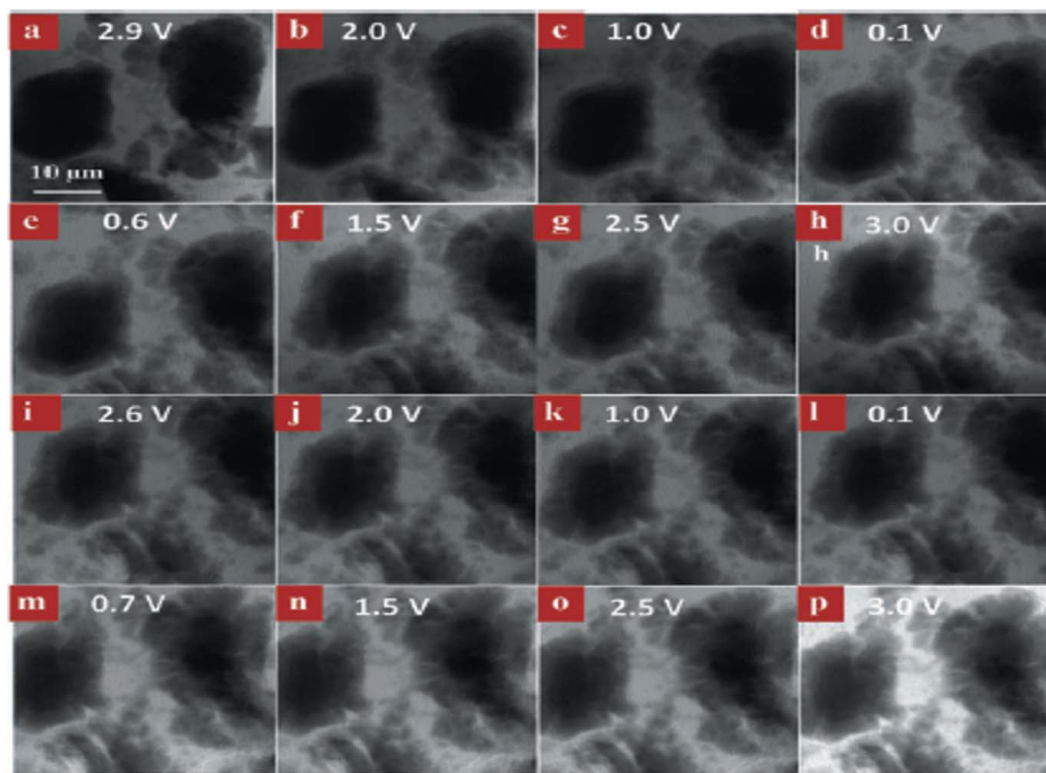
Figure 12
The morphology evolution of the CuO electrode during the first (*a–h*) and second cycle (*i–p*). Reproduced from Wang, Chen-Wiegart *et al.* (2013) with permission from The Royal Society of Chemistry.

during idle periods, especially for large samples (Teki *et al.*, 2009). After the rest period, the sample was firstly de-lithiated [Figs. 12(*e*)–12(*h*)]. Some cracks appear within the shell and extend along the radial direction toward the dark core. The formation of these cracks results from the existence of tension stress due to the volume change and lithium extracted during de-lithiation, which is consistent with the results of *in situ* TEM studies. However, the volume change of this large CuO particle during the first de-lithiation process is negligible and no obvious shrinking occurred, indicating that only a few lithium ions were extracted; this is very consistent with the weak oxidation peaks in the electrochemistry study described above. After this first cycle, the inner unreacted CuO was exposed to electrolytes due to the formation of many cracks within the shell, which allowed the active materials to undergo a further lithiation reaction during the second cycle [Figs. 12(*i*)–12(*l*)], though this process was much more limited than in the first cycle. Therefore, the shell became thicker and a few more cracks were formed toward the shrinking core during the second de-lithiation [Figs. 12(*m*)–12(*p*)].

The distributions of different phases (CuO, Cu_2O and Cu) within the sample under *in situ* electrochemistry conditions were analyzed by least-squares linear combination fitting. Fig. 13 shows the phase mappings, line profiles and composition of the active material during cycling. The fresh sample shows a major CuO phase with a small amount of Cu_2O (Fig. 13*a*). After the first lithiation, the large CuO particle was reduced from the outer surface to the inner core, so the phase

mapping shows a core (CuO)–shell (Cu) structure with an interface phase (Cu_2O) (Fig. 13*b*). During the following rest and anodic scanning, the shell became thicker (Fig. 13*c*). The mapping shows the result of the combination process, including the lithium ion equilibrium, self-reaction during the rest period (the rising of open circuit potential) and the following delithiation to form Cu_2O (anodic scanning). It was also confirmed by the line profile that an increase in Cu_2O from 25% to 40% occurred. During the second lithiation, the electrochemical reaction mainly occurred at the shell, where the Cu_2O in the shell became the main active material. As shown in the mapping (Fig. 13*d*), some Cu_2O in the shell was reduced to Cu, and the line profile shows a decrease in Cu_2O from 40% to 20%. During the second delithiation, the sample shows a poorer reversibility due to the large volume change and widespread structural damage; thus no obvious phase change was observed (not shown here).

It is more indispensable to couple *in situ* TXM imaging and XANES phase analysis in order to elucidate an *in situ* conversion reaction mechanism of a typical LIB material so that lithiated–delithiated CuO can be determined more accurately. The resultant morphology evolution, chemical phase change and detailed composition information on CuO anodes strongly suggest a size-dependent and core–shell lithiation–delithiation mechanism from the combination of these two techniques (Wang, Chen-Wiegart *et al.*, 2013).

Besides the above examples, an *in situ* TXM imaging tool can detect dendrite growth at the electrode surface. The main
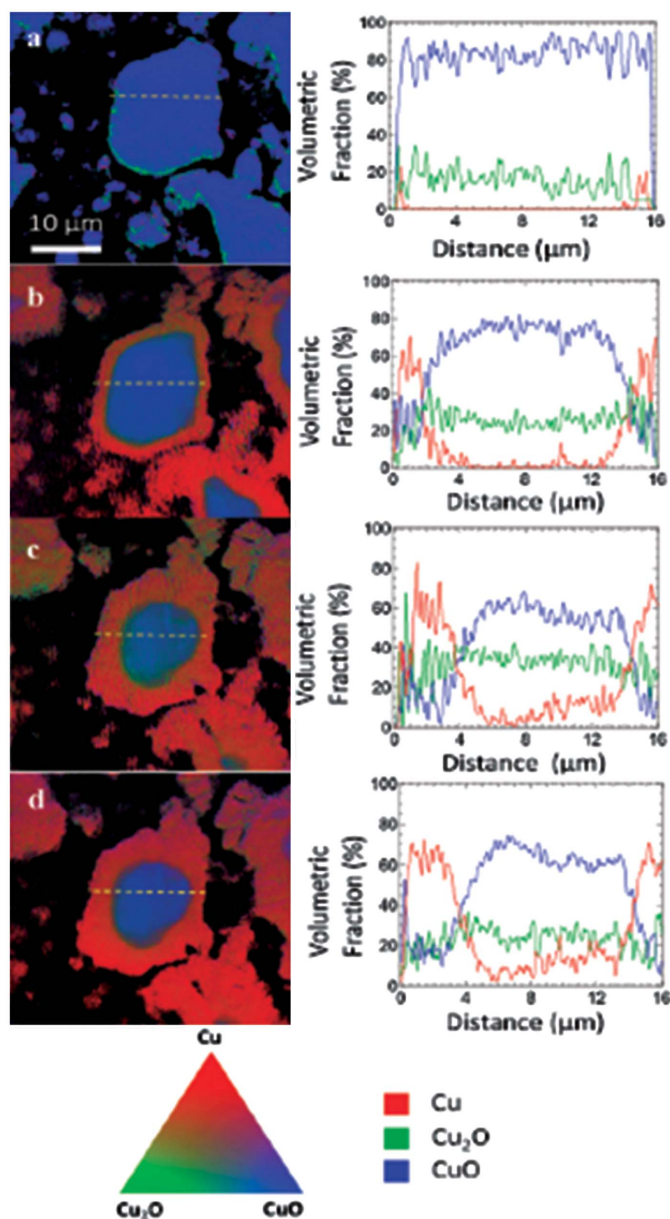
Figure 13
(*a*) Chemical phase mappings of CuO during cycling. (*b*) Line profiles of the corresponding particle during cycling. See text for details. Reproduced from Wang, Chen-Wiegart *et al.* (2013) with permission from The Royal Society of Chemistry.

challenges at the anode/electrolyte interface involve the formation of a SEI layer and the evolution of Li-metal dendrites in LIBs. The growth of Li-metal dendrites can contribute to an increase in the rate of capacity fading, *i.e.* due to the formation of 'dead Li' that leads to electrical contact with the electrode and causes internal short circuits through contact with the cathode (Mehdi *et al.*, 2015). Several efforts have endeavored to prevent dendrite growth primarily through using the appropriate electrolyte (Tatsuma *et al.*, 1999), additives (Ribes *et al.*, 1996; Zhang, 2006) and optimized separators (Ryou *et al.*, 2012). Nevertheless, their success has been limited. This suggests that in order to implement safe rechargeable lithium electrodes the empirical

approach of testing should be complemented with experiments aiming at identifying different growth modes and mechanisms (Steiger *et al.*, 2014). Consequently, different types of *in situ* techniques are used to study dendrite formation in lithium batteries such as optical and electron microscopy (OM/EM) (Gireaud *et al.*, 2006; Rosso *et al.*, 2006), nuclear magnetic resonance (NMR) (Bhattacharyya *et al.*, 2010), magnetic resonance imaging (MRI) (Harry *et al.*, 2014; Chandrashekar *et al.*, 2012) and *operando* electrochemical (S)TEM (Mehdi *et al.*, 2015). These techniques have the ability to detect 'tree-like' or 'moss-like' structures that emanate from the lithium surface and protrude into the electrolyte, even though they have drawbacks (Tatsuma *et al.*, 2001). The drawbacks of the aforementioned tools, such as indirect observation in NMR, the requirement of high-vacuum operation, possible electron beam damage by SEM and TEM, and insufficient spatial resolution of OM, can be resolved through *in situ* TXM. Pioneering work by Cheng *et al.* (2017) realised the high quality with high spatial resolution achieved with the help of *in operando* TXM in order to observe real-time Li-dendrite growth using an in-house-developed *in situ* cell. A recent review compiled various types of *in situ* methods for LIBs since 2009 (Harks *et al.*, 2015). However, the current report has focused only on *in situ* electrochemical synchrotron EXAFS, XANES, XRD and TXM for LIBs, to thoroughly illustrate surface, interface and bulk phase phenomena during operation, supported by scientific experiments and summarized in Table 1.

5. Future perspective

The application of *in situ* electrochemical synchrotron radiation methods to investigate battery materials plays an important role in their fundamental understanding. Major developments have taken place in recent years, particularly in the development of techniques that enable spatially resolved measurements. It is clear from various reviews that there are several techniques still in the development stage. Thus, research should be conducted in order to fill this gap in order to improve the current conventional methods for LIB research. To do so, highly improved synchrotron radiation techniques in terms of temporal, spatial and energy resolution are quite essential for future research. Among the decisive development of synchrotron radiation technology worldwide, the Taiwan government established the Synchrotron Radiation Research Center in 1983, later reorganized under the National Synchrotron Radiation Research Center (NSRRC) in 2003, to begin the planning of a national synchrotron facility for VUV and soft X-ray research. Accordingly, the Taiwan Light Source (TLS) was commissioned for user operation in October 1993 (Chang & Chen, 2013), the first third-generation synchrotron light source in Asia, located at NSRRC, Hsinchu. Three beamlines were initially constructed for when TLS opened to synchrotron users with 1.3 GeV of beam energy and 200 mA beam current. The electron beam energy of the TLS storage ring was upgraded to 1.5 GeV in 1996 (Su-Yu Chiang, 2007) which still does not fully satisfy the needs of researchers.

Table 1
Various *in situ* electrochemical-synchrotron radiation techniques reviewed in this paper.

	XAS	XRD	TXM
Studied parameters	Electronic, phase and composition change, SEI characterization	Phase transition and electro-chemical reaction	Morphological evolution, phase transformation and composition change
Referenced work	(Choi *et al.*, 2002; Nam, Yoon *et al.*, 2009; Nam, Wang *et al.*, 2009; Chen *et al.*, 2009; Liu, Liu *et al.*, 2014; Möller *et al.*, 2003; Ota *et al.*, 2003; Balasubramanian *et al.*, 2002; Wang *et al.*, 2017)	(Nam, Yoon *et al.*, 2009; Nam, Wang *et al.*, 2009; Liu, He *et al.*, 2014; Xu *et al.*, 2012; He *et al.*, 2013; Chao, Yen *et al.*, 2011; Chao *et al.*, 2010; Teki *et al.*, 2009; Wang *et al.*, 2017)	(Wang, Chen-Wiegart *et al.*, 2013; Nelson *et al.*, 2013; Chao, Yen *et al.*, 2011; Chao *et al.*, 2010; Cheng *et al.*, 2017)

Table 2
Basic parameters of the storage rings of the TLS and TPS synchrotron facilities (Chang & Chen, 2013).

	Storage ring	
Parameters	TLS	TPS
Energy (GeV)	1.5	3
Beam current (mA)	360	500
Circumference (m)	120	518.4
Cell/structure	6/TBA	24/DBA
Straight section length (m) × number	6 × 6	12 × 6 and 7 × 18
Natural emittance (nm rad)	25.6	1.6
Betatron tune (x/y)	7.18/4.13	26.18/13.28
Radiofrequency (MHz)	499.654	499.654
Harmonic number	200	864
Bunch length σ_L (mm)	6.5	2.8

However, in order to cope with the immense competition in the international scientific arena, and the rapid development of the worldwide synchrotron light sources, the insufficient brightness of the present TLS in the hard X-ray region, near consumption of all the TLS beam ports, the increasing demand for even brighter synchrotron X-ray sources for top-notch research as strongly expressed in the users meeting, the NSRRC in recent years came up with the decision to construct the Taiwan Photon Source (TPS), by upgrading to 3–3.3 GeV electron energy, a low-emittance synchrotron storage ring which will offer one of the world's brightest synchrotron X-ray sources, provide cutting-edge experimental facilities and novel multidisciplinary scientific research opportunities, enhance world-class academic research, bringing Taiwan's scientific research into the 21st century. Table 2 indicates the key parameters and huge improvement in the storage rings of TLS and TPS. The new storage ring of TPS will be a combined-function magnets lattice structure with 10 nm rad emittance and will be located in the inner tunnel of the TPS storage ring. The light source and its experimental facilities have been opened to the academic and scientific communities to conduct advanced research since 2016.

The construction of TPS was identified by a bright source of X-rays aimed at providing and generating an exhilarating vision of Taiwan's scientific and technological developments that go beyond the investigation and exploration of the reaction mechanism in LIBs reviewed in this paper and similar phenomena. In general, TPS will be one of the brightest synchrotron light sources in the world to implement an advanced and interdisciplinary experimental facility, open innovative experimental techniques, expand fields of scientific research in energy, biomedicine and nanoscience technologies, and optimize production that can in turn improve the country's international competitiveness in knowledge economy and attract more international research groups to perform experiments, offering the opportunity to build exclusive beamlines by providing beam ports and promoting international cooperation (Chang & Chen, 2013; Su-Yu Chiang, 2007).

6. Conclusion

Power fading and safety concerns regarding high-power Li-ion cells are the major technical barriers to meeting the challenging requirements for mobile, laptop, electric vehicle and hybrid electric vehicle applications. Safety concerns are related to the occurrence of exothermic reactions in charged batteries at elevated temperatures, which ultimately result in thermal runaway and catastrophic battery failure. In addition to the electrochemical characterization (excluding synchrotron radiation) of LIBs, *in situ* electrochemical-synchrotron radiation techniques can provide clear electronic structure, crystallographic structure and image-supported reaction mechanisms during charging and discharging. Among the techniques reviewed in this paper, the XAS results provide clear near-surface and bulk structural information of cathode materials. By contrast, XRD results demonstrate the structural changes observed in LIBs. The electronic and structural changes during charging and discharging can also be imaged using TXM. All the methods investigated in this paper produce results consistent with the surface and interface characterization of LIBs. On the basis of the selected works, we can conclude that the selected techniques have high promise for exploring and demonstrating reaction mechanisms in rechargeable batteries through quantitative, qualitative and imaging approaches. In summary, *in situ* electrochemical-synchrotron radiation is an exciting modern technology for characterizing real-time operations in LIBs.

Acknowledgements

topical reviews

References

Andersson, A. & Edström, K. (2001). *J. Electrochem. Soc.* **148**, A1100–A1109.

Andersson, A. S., Kalska, B., Häggström, L. & Thomas, J. O. (2000). *Solid State Ion.* **130**, 41–52.

Araki, K. & Sato, N. (2003). *J. Power Sources*, **124**, 124–132.

Arora, P., White, R. E. & Doyle, M. (1998). *J. Electrochem. Soc.* **145**, 3647–3667.

Ates, M. N., Mukerjee, S. & Abraham, K. (2014). *J. Electrochem. Soc.* **161**, A355–A363.

Aurbach, D., Zinigrad, E., Teller, H. & Dan, P. (2000). *J. Electrochem. Soc.* **147**, 1274–1279.

Balasubramanian, M., Lee, H. S., Sun, X., Yang, X.-Q., Moodenbaugh, A., McBreen, J., Fischer, D. A. & Fu, Z. (2002). *Electrochem. Solid-State Lett.* **5**, A22–A25.

Balasubramanian, M., Sun, X., Yang, X. & McBreen, J. (2001). *J. Power Sources*, **92**, 1–8.

Bashash, S., Moura, S. J. & Fathy, H. K. (2011). *J. Power Sources*, **196**, 8747–8754.

Bhattacharyya, R., Key, B., Chen, H., Best, A. S., Hollenkamp, A. F. & Grey, C. P. (2010). *Nat. Mater.* **9**, 504–510.

Bleith, P., van Beek, W., Kaiser, H., Novák, P. & Villevieille, C. (2015). *J. Phys. Chem. C*, **119**, 3466–3471.

Blyth, R. I. R., Buqa, H., Netzer, F. P., Ramsey, M. G., Besenhard, J. O., Golob, P. & Winter, M. (2000). *Appl. Surf. Sci.* **167**, 99–106.

Bramnik, N. N., Bramnik, K. G., Nikolowski, K., Hinterstein, M., Baehtz, C. & Ehrenberg, H. (2005). *Electrochem. Solid-State Lett.* **8**, A379–A381.

Bréger, J., Jiang, M., Dupré, N., Meng, Y. S., Shao-Horn, Y., Ceder, G. & Grey, C. P. (2005). *J. Solid State Chem.* **178**, 2575–2585.

Chandrashekar, S., Trease, N. M., Chang, H. J., Du, L.-S., Grey, C. P. & Jerschow, A. (2012). *Nat. Mater.* **11**, 311–315.

Chang, H.-H., Chang, C.-C., Wu, H.-C., Yang, M.-H., Sheu, H.-S. & Wu, N.-L. (2008). *Electrochem. Commun.* **10**, 335–339.

Chang, S.-L. & Chen, C.-T. (2013). *Synchrotron Radiat. News*, **26**, 32–38.

Chao, S.-C., Song, Y.-F., Wang, C.-C., Sheu, H.-S., Wu, H.-C. & Wu, N.-L. (2011). *J. Phys. Chem. C*, **115**, 22040–22047.

Chao, S.-C., Yen, Y.-C., Song, Y.-F., Chen, Y.-M., Wu, H.-C. & Wu, N.-L. (2010). *Electrochem. Commun.* **12**, 234–237.

Chao, S.-C., Yen, Y.-C., Song, Y.-F., Sheu, H.-S., Wu, H.-C. & Wu, N.-L. (2011). *J. Electrochem. Soc.* **158**, A1335–A1339.

Chen, Q., Wang, J., Tang, Z., He, W., Shao, H. & Zhang, J. (2007). *Electrochim. Acta*, **52**, 5251–5257.

Chen, Y., Zhao, Y., An, X., Liu, J., Dong, Y. & Chen, L. (2009). *Electrochim. Acta*, **54**, 5844–5850.

Cheng, J.-H., Assegie, A. A., Huang, C.-J., Lin, M.-H., Tripathi, A. M., Wang, C.-C., Tang, M.-T., Song, Y.-F., Su, W.-N. & Hwang, B.-J. (2017). *J. Phys. Chem. C*, **121**, 7761–7766.

Choi, H. C., Lee, S. Y., Kim, S. B., Kim, M. G., Lee, M. K., Shin, H. J. & Lee, J. S. (2002). *J. Phys. Chem. B*, **106**, 9252–9260.

Choi, N., Chen, Z., Freunberger, S. A., Ji, X., Sun, Y., Amine, K., Yushin, G., Nazar, L. F., Cho, J. & Bruce, P. G. (2012). *Angew. Chem. Int. Ed.* **51**, 9994–10024.

Crowther, O. & West, A. C. (2008). *J. Electrochem. Soc.* **155**, A806–A811.

De Groot, F. & Kotani, A. (2008). *Core Level Spectroscopy of Solids.* Boca Raton: CRC Press.

Domantovskii, A., Gurovich, B. & Maslakov, K. (2006). *Crystallogr. Rep.* **51**, S196–S199.

Du, X., He, W., Zhang, X., Yue, Y., Liu, H., Zhang, X., Min, D., Ge, X. & Du, Y. (2012). *J. Mater. Chem.* **22**, 5960–5969.

Fischer, D. & DeKoven, B. (1996). *DOW/NIST Materials Characterization Facility at U7A*. National Synchrotron Light Source Newsletter, pp. 6–7.

Galoisy, L., Cormier, L., Calas, G. & Briois, V. (2001). *J. Non-Cryst. Solids*, **293–295**, 105–111.

Gauthier, M., Carney, T. J., Grimaud, A., Giordano, L., Pour, N., Chang, H.-H., Fenning, D. P., Lux, S. F., Paschos, O., Bauer, C., Maglia, F., Lupart, S., Lamp, P. & Shao-Horn, Y. (2015). *J. Phys. Chem. Lett.* **6**, 4653–4672.

Giorgetti, M., Passerini, S., Smyrl, W. H., Mukerjee, S., Yang, X. & McBreen, J. (1999). *J. Electrochem. Soc.* **146**, 2387–2392.

Gireaud, L., Grugeon, S., Laruelle, S., Yrieix, B. & Tarascon, J. M. (2006). *Electrochem. Commun.* **8**, 1639–1649.

Giuli, G., Eeckhout, S. G., Paris, E., Koeberl, C. & Pratesi, G. (2005). *Meteorit. Planet. Sci.* **40**, 1575–1580.

Groot, F. de, Vankó, G. & Glatzel, P. (2009). *J. Phys. Condens. Matter*, **21**, 104207.

Harks, P., Mulder, F. & Notten, P. (2015). *J. Power Sources*, **288**, 92–105.

Harry, K. J., Hallinan, D. T., Parkinson, D. Y., MacDowell, A. A. & Balsara, N. P. (2014). *Nat. Mater.* **13**, 69–73.

He, H., Liu, Y., Liu, Q., Li, Z., Xu, F., Dun, C., Ren, Y., Wang, M. & Xie, J. (2013). *J. Electrochem. Soc.* **160**, A793–A804.

He, P., Yu, H., Li, D. & Zhou, H. (2012). *J. Mater. Chem.* **22**, 3680–3695.

Kaulich, B., Gianoncelli, A., Beran, A., Eichert, D., Kreft, I., Pongrac, P., Regvar, M., Vogel-Mikuš, K. & Kiskinova, M. (2009). *J. R. Soc. Interface*, **6**, S641–S647.

Kim, M. G., Shin, H. J., Kim, J.-H., Park, S.-H. & Sun, Y.-K. (2005). *J. Electrochem. Soc.* **152**, A1320–A1328.

Kim, S., Zhang, Z., Wang, S., Yang, L., Cairns, E. J., Penner-Hahn, J. E. & Deb, A. (2016). *J. Phys. Chem. C*, **120**, 7005–7012.

Kojima, T., Ishizu, T., Horiba, T. & Yoshikawa, M. (2009). *J. Power Sources*, **189**, 859–863.

Kong, F., Kostecki, R., Nadeau, G., Song, X., Zaghib, K., Kinoshita, K. & McLarnon, F. (2001). *J. Power Sources*, **97–98**, 58–66.

Koningsberger, D. C., Mojet, B. L., van Dorssen, G. E. & Ramaker, D. E. (2000). *Top. Catal.* **10**, 143–155.

Laruelle, S., Poizot, P., Baudrin, E., Briois, V., Touboul, M. & Tarascon, J. M. (2001). *J. Power Sources*, **97–98**, 251–253.

Li, G., Kudo, Y., Liu, K.-Y., Azuma, H. & Tohda, M. (2002). *J. Electrochem. Soc.* **149**, A1414.

Li, L.-H., Yau, S. & Dow, W.-P. (2016). *Electrochem. Commun.* **70**, 1–4.

Lipson, A. L., Ginder, R. S. & Hersam, M. C. (2011). *Adv. Mater.* **23**, 5613–5617.

Liu, Q., He, H., Li, Z.-F., Liu, Y., Ren, Y., Lu, W., Lu, J., Stach, E. A. & Xie, J. (2014). *Appl. Mater. Interfaces*, **6**, 3282–3289.

Liu, Q., Liu, Y., Sun, C.-J., Li, Z., Ren, Y., Lu, W., Stach, E. A. & Xie, J. (2014). *Electrochim. Acta*, **136**, 318–322.

McArthur, M., Trussler, S. & Dahn, J. (2012). *J. Electrochem. Soc.* **159**, A198–A207.

McBreen, J. (2009). *J. Solid State Electrochem.* **13**, 1051–1061.

Mansour, A., Smith, P., Baker, W., Balasubramanian, M. & McBreen, J. (2003). *J. Electrochem. Soc.* **150**, A403–A413.

Mehdi, B. L., Qian, J., Nasybulin, E., Park, C., Welch, D. A., Faller, R., Mehta, H., Henderson, W. A., Xu, W., Wang, C. M., Evans, J. E., Liu, J., Zhang, J. G., Mueller, K. T. & Browning, N. D. (2015). *Nano Lett.* **15**, 2168–2173.

Molenda, J., Ojczyk, W. & Marzec, J. (2007). *J. Power Sources*, **174**, 689–694.

Molenda, J., Ojczyk, W., Świerczek, K., Zając, W., Krok, F., Dygas, J. & Liu, R.-S. (2006). *Solid State Ion.* **177**, 2617–2624.

Möller, K. C., Santner, H. J., Kern, W., Yamaguchi, S., Besenhard, J. O. & Winter, M. (2003). *J. Power Sources*, **119–121**, 561–566.

Morcrette, M., Chabre, Y., Vaughan, G., Amatucci, G., Leriche, J. B., Patoux, S., Masquelier, C. & Tarascon, J. M. (2002). *Electrochim. Acta*, **47**, 3137–3149.

Nakai, I., Shiraishi, Y. & Nishikawa, F. (1999). *At. Spectrosc.* **54**, 143–149.

Nam, K.-W., Wang, X.-J., Yoon, W.-S., Li, H., Huang, X., Haas, O., Bai, J. & Yang, X.-Q. (2009). *Electrochem. Commun.* **11**, 913–916.

Nam, K.-W., Yoon, W.-S., Zaghib, K., Yoon Chung, K. & Yang, X.-Q. (2009). *Electrochem. Commun.* **11**, 2023–2026.

Nelson, J., Yang, Y., Misra, S., Andrews, J. C., Cui, Y. & Toney, M. F. (2013). *Proc. SPIE*, **8851**, 88510B.

Ota, H., Akai, T., Namita, H., Yamaguchi, S. & Nomura, M. (2003). *J. Power Sources*, **119–121**, 567–571.

Peled, E. (1979). *J. Electrochem. Soc.* **126**, 2047–2051.

Peled, E., Golodnttsky, D., Ardel, G., Menachem, C., Bar Tow, D. & Eshkenazy, V. (2011). *MRS Proc.* **393**, doi:10.1557/PROC-393-209.

Raccichini, R., Varzi, A., Passerini, S. & Scrosati, B. (2015). *Nat. Mater.* **14**, 271–279.

Rehr, J. J. & Albers, R. C. (2000). *Rev. Mod. Phys.* **72**, 621–654.

Rosso, M., Brissot, C., Teyssot, A., Dollé, M., Sannier, L., Tarascon, J.-M., Bouchet, R. & Lascaud, S. (2006). *Electrochim. Acta*, **51**, 5334–5340.

Ryou, M. H., Lee, D. J., Lee, J. N., Lee, Y. M., Park, J. K. & Choi, J. W. (2012). *Adv. Energ. Mater.* **2**, 645–650.

Schnohr, C. & Ridgway, M. (2015). *X-ray Absorption Spectroscopy of Semiconductors.* Berlin: Springer.

Schranzhofer, H., Bugajski, J., Santner, H. J., Korepp, C., Möller, K. C., Besenhard, J. O., Winter, M. & Sitte, W. (2006). *J. Power Sources*, **153**, 391–395.

Shin, H. C., Chung, K. Y., Min, W. S., Byun, D. J., Jang, H. & Cho, B. W. (2008). *Electrochem. Commun.* **10**, 536–540.

Sina, M., Nam, K. W., Su, D., Pereira, N., Yang, X. Q., Amatucci, G. G. & Cosandey, F. (2013). *J. Mater. Chem. A*, **1**, 11629–11640.

Singh, G., West, W., Soler, J. & Katiyar, R. S. (2012). *J. Power Sources*, **218**, 34–38.

Sloop, S. E., Pugh, J. K., Wang, S., Kerr, J. & Kinoshita, K. (2001). *Electrochem. Solid-State Lett.* **4**, A42–A44.

Steiger, J., Kramer, D. & Mönig, R. (2014). *Electrochim. Acta*, **136**, 529–536.

Su-Yu Chiang, D. L. & a, M.-T. L. (2007). *Synchrotron Radiat. News*, **20**, 2–7.

Tarascon, J.-M. (2010). *Philos. Trans. R. Soc. A*, **368**, 3227–3241.

Tatsuma, T., Taguchi, M., Iwaku, M., Sotomura, T. & Oyama, N. (1999). *J. Electroanal. Chem.* **472**, 142–146.

Tatsuma, T., Taguchi, M. & Oyama, N. (2001). *Electrochim. Acta*, **46**, 1201–1205.

Teki, R., Datta, M. K., Krishnan, R., Parker, T. C., Lu, T. M., Kumta, P. N. & Koratkar, N. (2009). *Small*, **5**, 2236–2242.

Tudela Ribes, A., Beaunier, P., Willmann, P. & Lemordant, D. (1996). *J. Power Sources*, **58**, 189–195.

Wang, C., Liu, H. & Yang, W. (2012). *J. Mater. Chem.* **22**, 5281–5285.

Wang, F., Pradanawati, S. A., Yeh, N. H., Chang, S. C., Yang, Y. T., Huang, S. H., Lin, P. L., Lee, J. F., Sheu, H. S., Lu, M. L., Chang, C. K., Ramar, A. & Su, C. H. (2017). *Chem. Mater.* **29**, 5537–5549.

Wang, F., Wu, L., Key, B., Yang, X. Q., Grey, C. P., Zhu, Y. & Graetz, J. (2013). *Adv. Energ. Mater.* **3**, 1324–1331.

Wang, J., Chen-Wiegart, Y. & Wang, J. (2013). *Chem. Commun.* **49**, 6480–6482.

Wang, J., Karen Chen, Y., Yuan, Q., Tkachuk, A., Erdonmez, C., Hornberger, B. & Feser, M. (2012). *Appl. Phys. Lett.* **100**, 143107.

Wang, Q.-S., Sun, J.-H., Chu, G.-Q., Yao, X.-L. & Chen, C.-H. (2007). *J. Therm. Anal. Calorim.* **89**, 245–250.

Wang, W., Zhang, J., Jia, Z., Dai, C., Hu, Y., Zhou, J. & Xiao, Q. (2014a). *Phys. Chem. Chem. Phys.* **16**, 13858–13865.

Wang, W., Zhang, J., Jia, Z., Dai, C., Hu, Y., Zhou, J. & Xiao, Q. (2014b). *Phys. Chem. Chem. Phys.* **16**, 13858–13865.

Wang, X., Hanson, J. C., Frenkel, A. I., Kim, J.-Y. & Rodriguez, J. A. (2004). *J. Phys. Chem. B*, **108**, 13667–13673.

Wang, X., Yu, X., Li, H., Yang, X., McBreen, J. & Huang, X. (2008). *Electrochem. Commun.* **10**, 1347–1350.

Westre, T. E., Kennepohl, P., DeWitt, J. G., Hedman, B., Hodgson, K. O. & Solomon, E. I. (1997). *J. Am. Chem. Soc.* **119**, 6297–6314.

Willmott, P. R., Meister, D., Leake, S. J., Lange, M., Bergamaschi, A., Böge, M., Calvi, M., Cancellieri, C., Casati, N., Cervellino, A., Chen, Q., David, C., Flechsig, U., Gozzo, F., Henrich, B., Jäggi-Spielmann, S., Jakob, B., Kalichava, I., Karvinen, P., Krempasky, J., Lüdeke, A., Lüscher, R., Maag, S., Quitmann, C., Reinle-Schmitt, M. L., Schmidt, T., Schmitt, B., Streun, A., Vartiainen, I., Vitins, M., Wang, X. & Wullschleger, R. (2013). *J. Synchrotron Rad.* **20**, 667–682.

Xu, F., He, H., Liu, Y., Dun, C., Ren, Y., Liu, Q., Wang, M. & Xie, J. (2012). *J. Electrochem. Soc.* **159**, A678–A687.

Yamada, A., Kudo, Y. & Liu, K.-Y. (2001). *J. Electrochem. Soc.* **148**, A747.

Yamada, Y., Iriyama, Y., Abe, T. & Ogumi, Z. (2009). *Langmuir*, **25**, 12766–12770.

Ye, Y., Kawase, A., Song, M.-K., Feng, B., Liu, Y.-S., Marcus, M. A., Feng, J., Cairns, E. J., Guo, J. & Zhu, J. (2016). *Nanomaterials*, **6**, 14.

Yoon, W.-S., Balasubramanian, M., Chung, K. Y., Yang, X.-Q., McBreen, J., Grey, C. P. & Fischer, D. A. (2005). *J. Am. Chem. Soc.* **127**, 17479–17487.

Zabinsky, S., Rehr, J., Ankudinov, A., Albers, R. & Eller, M. (1995). *Phys. Rev. B*, **52**, 2995–3009.

Zhang, S. S. (2006). *J. Power Sources*, **162**, 1379–1394.